NANO LETTERS

Letter

pubs.acs.org/NanoLett

Magnetic Hysteresis in Er Trimers on Cu(111)

Aparajita Singha,[†] Fabio Donati,[†] Christian Wäckerlin,[†] Romana Baltic,[†] Jan Dreiser,[†,‡] Marina Pivetta,[†] Stefano Rusponi,[†] and Harald Brune*[,†]

[†]Institute of Physics, École Polytechnique Fédérale de Lausanne, Station 3, CH-1015 Lausanne, Switzerland

[‡]Swiss Light Source, Paul Scherrer Institute, CH-5232 Villigen PSI, Switzerland

Supporting Information

ABSTRACT: We report magnetic hysteresis in Er clusters on Cu(111) starting from the size of three atoms. Combining X-ray magnetic circular dichroism, scanning tunneling microscopy, and mean-field nucleation theory, we determine the size-dependent magnetic properties of the Er clusters. Er atoms and dimers are paramagnetic, and their easy magnetization axes are oriented in-plane. In contrast, trimers and bigger clusters exhibit magnetic hysteresis at 2.5 K with a relaxation time of 2 min at 0.1 T and out-of-plane easy axis. This appearance of magnetic stability for trimers coincides with their enhanced structural stability.

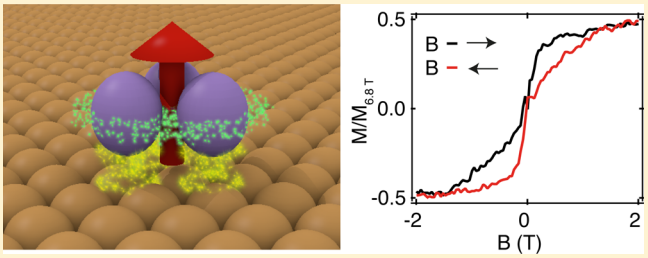

KEYWORDS: *Rare earth clusters, X-ray magnetic circular dichroism, scanning tunneling microscopy, superlattice, hysteresis, magnetic anisotropy*

The aim to explore the ultimate density limit of magnetic information storage has triggered the interest in surface-supported magnetic nanostructures.[1] Following the discovery of ferromagnetic order and remanence in monatomic Co chains[2] at 10 K, magnetic bistability was observed in clusters with as few as 12 and 5 Fe atoms[3,4] with magnetic lifetimes up to several hours below 0.5 K. However, for smaller clusters, significantly shorter lifetimes were reported at 0.3 K.[5,6] Increasing the lifetimes of small clusters, and preserving them up to higher temperatures, requires large magnetic anisotropy energy[7] (MAE) and protection from scattering with substrate conduction electrons. Rare earth atoms promise both: (i) their magnetic properties originate from the 4f orbitals, which are highly localized and well-screened from the conduction electrons and (ii) the high spin−orbit coupling within the 4f orbitals can give rise to an MAE which is higher than the one of 3d materials.[8]

Here we combine X-ray magnetic circular dichroism (XMCD), scanning tunneling microscopy (STM), and mean-field nucleation theory to determine the size-dependent magnetic properties of Er clusters. Erbium atoms exhibit in-plane magnetization due to the interaction with the underlying Cu(111) substrate.[9] The same is true for dimers. However, the easy axes for all bigger clusters are oriented out-of-plane due to the modified local ligand field environments. In addition, all clusters starting from trimers exhibit magnetic hysteresis with a relaxation time of 2 min at 2.5 K and 0.1 T.

The X-ray absorption spectra (XAS) were recorded at the EPFL/PSI X-Treme beamline at the Swiss Light Source.[10] We used circularly polarized light in an external magnetic field of 6.8 T at 2.5 K for the XMCD measurements (see Methods). The magnetic field was always collinear with the incident X-rays. XMCD probes the magnetic moment projected along the beam, and its amplitude provides information about the strength of the magnetic moment localized at the element under investigation. The Er coverage (Θ) is expressed in units of monolayer (ML), where one ML is defined as one Er atom per substrate Cu atom. To determine the polar anisotropy of the magnetization, we acquired XAS and XMCD at two incident angles, namely, normal ($\theta = 0°$) and grazing ($\theta = 55°$) to the surface.

Figures 1a,b show the coverage-dependent XAS at the M_5 edge, for normal and grazing incidence. Corresponding XMCD spectra were normalized to the total XAS integrated over the entire $M_{4,5}$ edge and are shown in Figures 1c,d. The XAS line shape is the characteristic of a $4f^{11}$ configuration[9,11] implying 3 holes in the valence shell, $n_h = 3$ independent of the coverage, and therefore a total angular momentum $J = \frac{15}{2}$ following Hund's rules. The invariance of n_h with Θ is concluded from the absence of spectral shifts[12] and from our multiplet simulations[19] (Figures S12, S13). The triple-peak feature at the M_5 edge corresponds to the dipole allowed transitions[13] ($\Delta J = 0, \pm 1$) from the filled 3d to the open 4f shell of Er. A monotonic increase (decrease) of the out-of-plane (in-plane) XMCD is observed with increasing Θ (Figures 1c,d). We applied sum rules to quantify the expectation values of the orbital and effective spin magnetic moments per atom projected

Received: December 21, 2015
Revised: May 4, 2016
Published: May 6, 2016

DOI: 10.1021/acs.nanolett.5b05214
Nano Lett. 2016, 16, 3475−3481

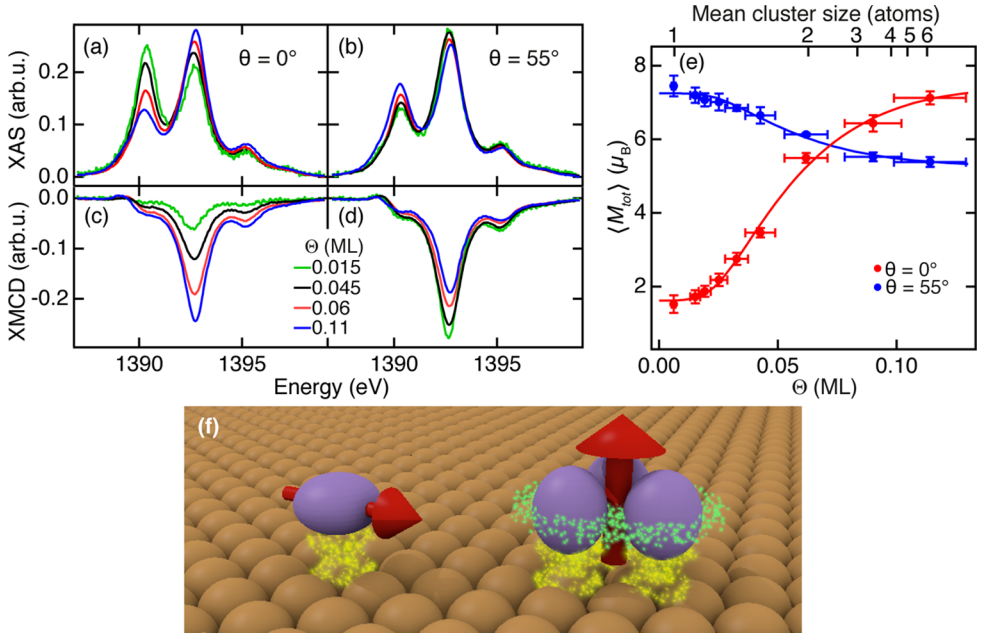

Figure 1. (a, b) Coverage dependent XAS and (c, d) XMCD at the M_5 Er edge in normal ($\theta = 0°$) and grazing ($\theta = 55°$) incidence ($T = 2.5$ K, $B = 6.8$ T). (e) Normal and grazing components of the total magnetic moment as a function of coverage (bottom) and mean cluster size (top), deduced from the XMCD sum rules assuming $n_h = 3$. Solid lines are fits with moments of atoms, dimers, and bigger clusters as fit parameters. (f) Schematic showing two regimes of magnetic anisotropy: in-plane magnetization for single atoms and out-of-plane easy axis for the Er trimers on Cu(111). Red arrows indicate the orientation of the easy axis. Speckles in yellow indicate the interaction between Er and Cu atoms, while the interaction among the Er atoms within a trimer is visualized by green speckles.

onto the beam axis, $\langle L \rangle$ and $\langle 2S + 6T \rangle$, respectively (Table S1).[14,15] Summing these moments, we obtain the expectation value of the effective total moment $\langle M_{tot}(\Theta) \rangle$ projected along the beam (Figure 1e). Apart from the $\langle 6T \rangle$ contribution, $\langle M_{tot} \rangle$ corresponds to $g\langle J \rangle$, with $g = 1.2$ the electron Landé factor. The out-of-plane projected component of $\langle M_{tot} \rangle$ increases gradually with Θ, reaching a maximum of 7.1 ± 0.2 μ_B/atom at 0.11 ML. This value is slightly lower than 8.0 μ_B/atom measured in Er crystals along the C-axis at 4.2 K.[16] We attribute this difference to the interaction with the Cu(111) substrate. Note that the invariance of n_h together with the strong spin−orbit coupling of Er implies that the modulus of J is coverage and thereby cluster size independent. This is a remarkable distinction of 4f with respect to 3d elements that display a strong size dependence of the orbital moments.[7,17]

The growing out-of-plane magnetization with increasing Er coverage can be rationalized by considering the modified effective ligand field created by the increased atomic coordinations at higher coverages. For rare earths, the magnetic ground states are closely related to the shape of the 4f charge distribution, which for Er is prolate for the maximum and oblate for the minimum possible out-of-plane magnetic moment.[18] The ligand field of the underlying Cu(111) substrate induces an oblate shape of the localized 4f charge distribution of single Er atoms, causing the in-plane magnetization observed at the lowest coverages.[9] In contrast, atoms within an Er cluster see the neighbors as equatorially placed charges. To minimize the electrostatic interaction with the ligands, the 4f charge distribution modifies to a prolate shape, leading to the observed increase in the out-of-plane magnetization (Figure 1f). This reorientation of the easy axis in the presence of equatorial ligands is further supported by our multiplet simulations (Figures S12, S13).

To explore the magnetic stability and to quantify the MAE of Er clusters of different size, we acquired magnetization curves by recording the field-dependent maximum XMCD at the M_5 edge (Figures 2a−e and Methods). No magnetic hysteresis is evident up to a coverage of 0.035 ML, at which the first butterfly shaped hysteresis becomes visible in normal incidence (inset in Figure 2b). The hysteresis area increases at higher coverages, and the magnetization curves start to exhibit remanence for $\Theta > 0.06$ ML (Figure 2e). The open hysteresis loop at the employed sweep rate of 12.5 mT/s indicates that the magnetization lifetime τ is longer than tens of seconds. To quantify τ, we first magnetized the sample at 3 T and subsequently reduced the field down to 0.1 T, where we recorded the temporal decay of the maximum XMCD. Exponential fits to these data indicate similar values of τ for 0.045 ML, $\tau = 114 \pm 19$ s, and for 0.06 ML, $\tau = 130 \pm 7$ s (Figures 3a,b). The measured τ is expected to be limited by the X-ray induced demagnetization[20] which can be relevant at the employed photon flux of 2×10^{10} photons mm^{-2} s^{-1}. Therefore, the reported values of τ represent the lower bound to the intrinsic magnetization lifetime. Note that distance-dependent magnetic interactions, e.g., dipolar and Ruderman−Kittel−Kasuya−Yosida (RKKY), are negligible in the present experimental conditions (see Methods), and therefore the reported magnetic properties are characteristics of individual atoms and clusters.

To identify the minimum cluster size that defines the onset of out-of-plane easy axis and of hysteresis, we characterized the growth of Er on Cu(111) using low-temperature STM. Figures 2f–j show STM images for coverages close to those of the magnetization curves. At the lowest coverage (0.02 ML), most of the Er atoms arrange in a honeycomb lattice with a period of 2.81 ± 0.04 nm (Figure 2f). With increase in coverage, we observe a long-range ordered hexagonal superlattice of $1.38 \pm$

DOI: 10.1021/acs.nanolett.5b05214
Nano Lett. 2016, 16, 3475−3481

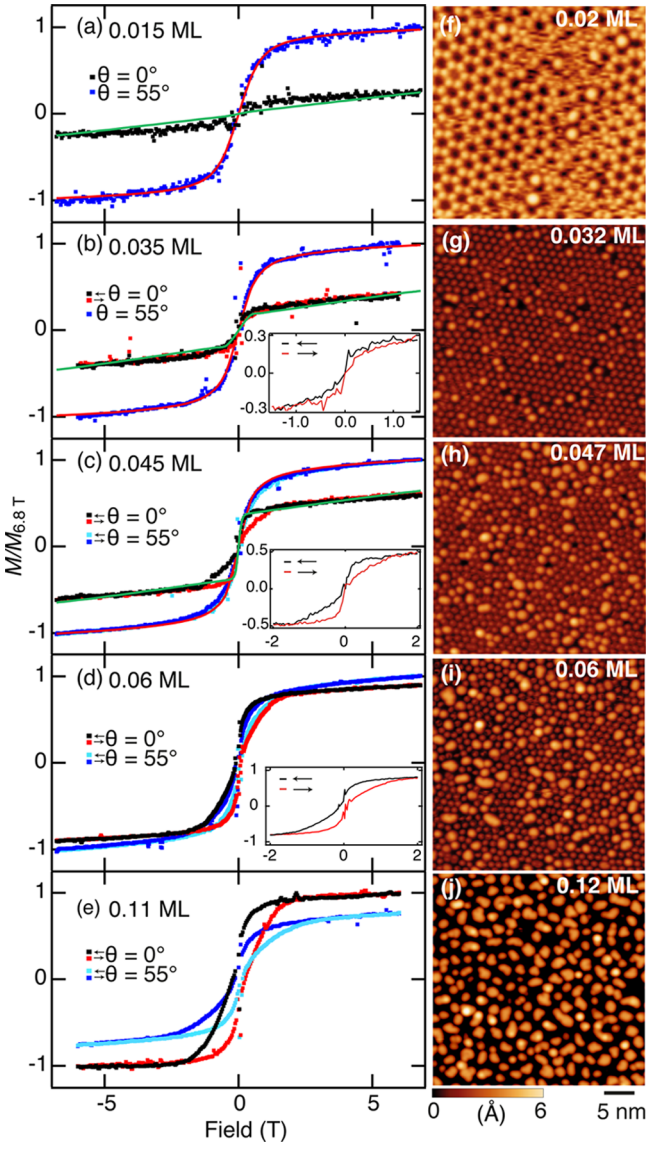

Figure 2. (a–e) Magnetization curves. Solid lines are the magnetization curves simulated assuming thermodynamic equilibrium, using the cluster size distributions deduced from the STM measurements and their magnetic properties, as described in the text. Insets in b–d show zooms of the magnetic hysteresis in normal incidence at the corresponding coverages (T = 2.5 K, $\dot{B}$ = 12.5 mT/s). (f–j) STM images at coverages close to the ones for which the magnetization curves (a–e) were recorded. For f–i, the deposition temperature was $T_d = 4 \pm 1$ K, and the STM measurement temperature was T = 4.4 K. The imaging parameters were: (V_t, I_t) = (1.8 V, 10 pA), (−30 mV, 100 pA), (−50 mV, 100 pA), and (−300 mV, 500 pA), respectively. For j: $T_d = 10 \pm 1$ K, T = 5 K, and (V_t, I_t) = (100 mV, 20 pA).

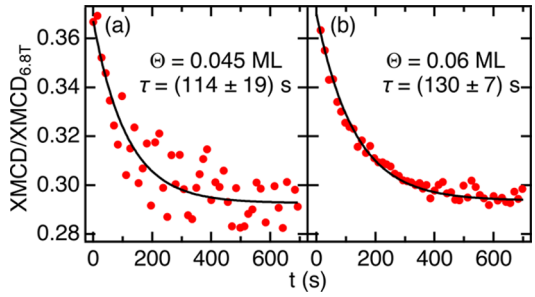

Figure 3. Measured time evolution of XMCD. Magnetic relaxation time $\tau = 114 \pm 19$ s and 130 ± 7 s respectively for 0.045 and 0.06 ML Er. Solid lines are exponential fits. (B = 0.1 T, T = 2.5 K, X-ray flux 2×10^{10} photons mm^{-2} s^{-1}, $\theta = 0°$).

0.04 nm period (Figure 2g). Adatom superlattices form on Ag(111) and Cu(111) surfaces due to a combination of short-range repulsion among the single atoms and long-range oscillatory interaction mediated by the surface state electrons.[21−25] While the former defines an effective barrier for cluster formation through lateral attachment of adatoms to each other, the first minimum of the latter dictates the equilibrium distance among the single atoms within the superlattice. In the present case, the period is slightly larger than for the formerly studied 3d elements on Cu(111)[21,22] but similar to the one reported for Ce on Cu(111),[23] due to a strong dipolar contribution to the short-range repulsions for the lanthanides. Note that a high tunnel resistance was crucial for non-perturbative imaging of the superlattices, as also observed for other rare earth superlattices on noble metal surfaces.[23−25]

The ordered structure of the superlattice is perturbed by Er clusters whose relative abundance and size increases with coverage (Figures 2h–j). To identify their size, we analyzed their characteristic shape and apparent height profiles. Figure 4a illustrates the shapes of the observed Er species as a function of the number of constituent atoms, N. These shapes are well-reproduced assuming 2D Gaussian profiles of the constituent atoms with their centers separated by the nearest neighbor distance of bulk Er (355 pm) (Figure 4b). In addition, the apparent height profiles clearly differentiate the N = 1, 2, and

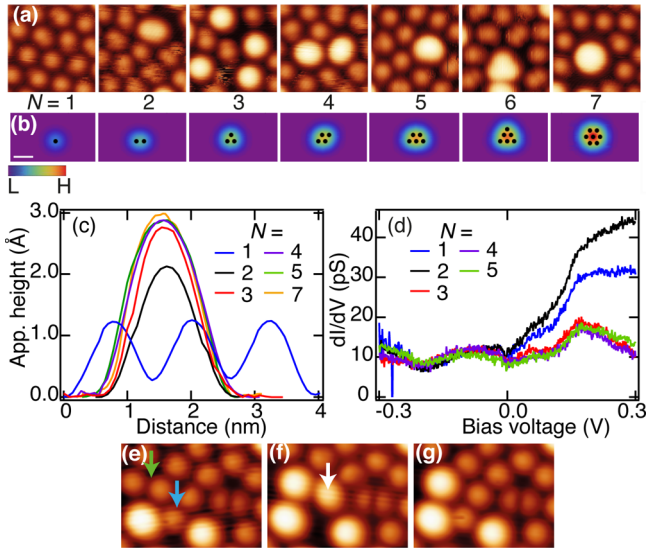

Figure 4. (a) Shape of the observed Er species with size of N atoms (image size: 5 × 5 nm^2, V_t = −30 mV, I_t = 100 pA). (b) Simulated shapes with the positions of the constituent atoms marked as black dots. Scale bar is 1 nm. (c) Apparent height profiles of different Er species. (d) STS measurements showing contrast in the electronic properties among N = 1, 2, and ≥3 species (V_t = −300 mV, I_t = 300 pA, lock-in modulation V_{mod} = 10 mV peak-to-peak at a frequency f = 2687 Hz). Sequence of STM images showing, from e to f: creation of a dimer (trimer) by atomic manipulations at the two locations marked with cyan (green) arrows in e; from g to h: the dimer splits into two monomers by applying 600 mV with the tip positioned at the white arrow. (Image size: 6 × 4.5 nm^2, V_t = −300 mV, I_t = 100 pA). T = 4.4 K for all frames.

DOI: 10.1021/acs.nanolett.5b05214
Nano Lett. 2016, 16, 3475−3481

≥3 species[4,6,26−28] (Figure 4c). These three size groups also possess distinct electronic properties as demonstrated by our scanning tunneling spectroscopy (STS) measurements (Figure 4d). Note that the tunnel current for these STS measurements is kept low to prevent current-induced adatom hopping.

A sharp contrast between N = 2 and ≥3 species is also evident from their distinct stability toward dissociation induced by the tunneling electrons from the STM tip. Figures 4e−g display a sequence of STM images showing the creation of a dimer and a trimer and the subsequent split of the dimer. The cluster formation is accomplished by approaching the tip with typical tunneling parameters (V_t = 10 mV, I_t = 10 pA) and subsequently increasing the set point current of the feedback loop until a sudden change in the tip height occurs. The dimer is split by applying 600 mV with the tip placed on top (Figure 4g). Trimers and larger clusters cannot be dissociated; they remain intact up to at least 2 V. These observations indicate that dimers are much less stable than all bigger clusters.

The distinct electronic and structural properties of N = 1, 2, and ≥3 species suggest the distinction of these three size classes in a first approach. From the apparent height histograms extracted from STM images (Figure S2a), we quantified their relative abundance. Their respective contributions to the XMCD is obtained by multiplying these abundances with their sizes, i.e., 1 and 2, for the monomers and dimers, and the mean size for all larger clusters. This gives the relative amount of Er present in the form of clusters containing N atoms, $Q_N(\Theta)$. In addition, we varied the deposition temperature (T_d = 4 ± 1 K and 10 ± 1 K) creating lower or higher relative amounts of $N \geq 3$ clusters by thermally activated adatom-to-cluster attachment. Q_N are shown in Figure 5a and b for the two deposition temperatures. Note that by definition they always add up to 100% for a given coverage Θ. From 0.03 ML onward, $Q_{\geq 3}$ is higher for T_d = 10 ± 1 K.

Since the STM and XMCD measurements were not taken at the same coverages, and with the aim of achieving a more quantitative understanding of the growth of this system, we simulated the observed trends of $Q_N(\Theta)$ by modeling the nucleation and growth with rate equations from mean-field nucleation theory. This model accounts for the particularities of the present system, namely, the presence of an attachment barrier as well as the large and coverage-dependent cross sections for nucleation by direct impingement[29,30] (see SI). Solid lines in Figures 5a and b show that this model reproduces the experimental results very well for both temperatures, evidently with a single set of parameters (see SI).

The knowledge of $Q_N(\Theta)$ allows us to quantify the expectation value of the magnetic moment/atom $\langle M_N \rangle$ for each cluster size N and for normal and grazing incidence. For this we fit the measured $\langle M_{tot}(\Theta) \rangle$ using $\langle M_{tot}(\Theta) \rangle = \sum_{N=1,2,\geq 3} \langle M_N \rangle \, Q_N(\Theta)$ (solid lines in Figure 1e) and obtain the six values on the left-hand side of Table 1. In addition, we fit the full magnetization curves with a semiclassical model assuming (a) a constant modulus of the total moment/atom, (b) ferromagnetic exchange coupling within a cluster, and (c) having the magnetic anisotropies/atom K_N as the only parameters (Figures 2a−c, S8, and Methods). Note that these are two independent approaches. We find larger in-plane than out-of-plane moments for $N \leq 2$. This is in agreement with the corresponding negative K_N and implies an out-of-plane hard axis for these species. In contrast, clusters with $N \geq 3$ possess larger out-of-plane moment and positive K_N, indicating an out-of-plane easy axis. Note that the MAE/atom of the Er dimers is significantly lower than the one of the single atoms, in contrast to what has been reported for Gd dimers on the same substrate.[26]

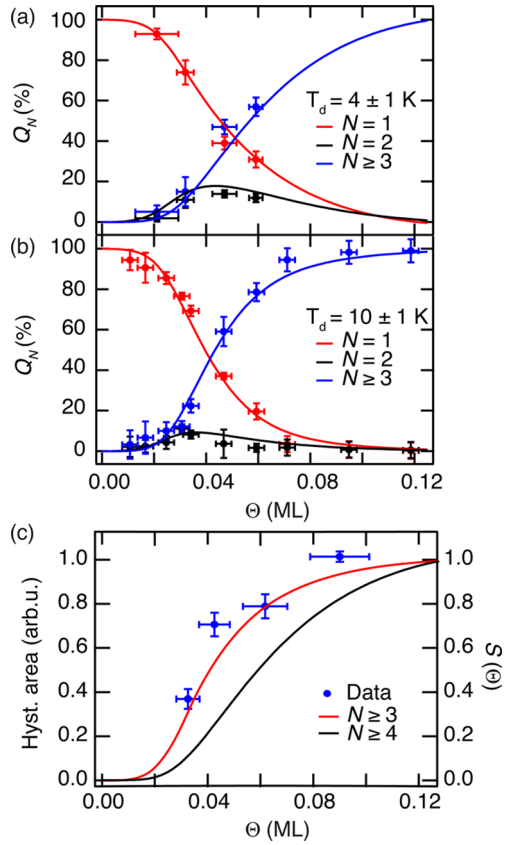

Figure 5. Coverage dependence of Q_N, the fraction of Er present in N-sized cluster for Er deposition at (a) 4 K and (b) 10 K. Dots: data deduced from the apparent heights in the STM images; full lines: results from mean-field nucleation theory with the parameters discussed in the text. (c) Comparison of the hysteresis area (dots) with the weighted contribution to the total XMCD in normal incidence, $S(\Theta)$, for $N \geq 3$ and $N \geq 4$ (full lines).

Table 1. Magnetic Moment ($\langle M_N \rangle$) and Anisotropy (K_N) of the Three Cluster Sizes[a]

N	$\langle M_N \rangle$ θ = 0° (μ_B/atom)	$\langle M_N \rangle$ θ = 55° (μ_B/atom)	anisotropy K_N (meV/atom)	orientation of easy axis/plane
1	1.6 ± 0.1	7.2 ± 0.1	−9.9 ± 0.9	in-plane
2	4.6 ± 0.8	6.4 ± 0.8	−1.9 ± 0.5	in-plane
≥3	7.2 ± 0.2	5.3 ± 0.2	2.9 ± 0.5	out-of-plane

[a] $\langle M_N \rangle$ and K_N are calculated from the fit of $\langle M_{tot}(\Theta) \rangle$, and of the magnetization curves, respectively.

Finally, to identify the minimum cluster size that causes magnetic hysteresis, we quantified the coverage-dependent area of the hysteresis loops at θ = 0° (Figure 5c). Since the magnetization is in-plane for $N \leq 2$ while the maximum opening of the hysteresis is observed in the out-of-plane direction, monomers and dimers cannot be the origin of hysteresis. To understand whether N = 3 belongs to the size group causing hysteresis, we extended our nucleation and growth model to the case of four populations (N = 1, 2, 3 and ≥4). A careful analysis of the apparent cluster heights and shapes allows us to clearly distinguish the trimers from $N \geq 4$ species (see SI). The fractions of Er present in the respective cluster size classes, $Q_N(\Theta)$, obtained from this model are in

DOI: 10.1021/acs.nanolett.5b05214
Nano Lett. 2016, 16, 3475−3481

excellent agreement with the experimental observations (Figure S7). We employ this model to fit $\langle M_{tot}(\Theta)\rangle$ with known values of $\langle M_1\rangle$ and $\langle M_2\rangle$ while using only $\langle M_3\rangle$ and $\langle M_{\geq 4}\rangle$ as fit parameters (Figure S8). In agreement with the three population growth model, we obtain out-of-plane magnetic orientation for the trimers and bigger clusters.

In order to correlate the onset of hysteresis with the appearance of a given cluster size, we calculated the contributions to the out-of-plane XMCD from clusters with $N \geq 3$ and $N \geq 4$ weighted by their relative abundance $Q_N(\Theta)$. We define this as $S(\Theta)$, where

$$S(\Theta) = \begin{cases} Q_{\geq 3}(\Theta)\dfrac{\langle M_{\geq 3}\rangle}{\langle M_{tot}(\Theta)\rangle} & \text{for } N \geq 3 \\ Q_{\geq 4}(\Theta)\dfrac{\langle M_{\geq 4}\rangle}{\langle M_{tot}(\Theta)\rangle} & \text{for } N \geq 4 \end{cases} \quad (1)$$

Here $\langle M_{\geq 3}\rangle$ and $\langle M_{\geq 4}\rangle$ are the values obtained from the fits of $\langle M_{tot}(\Theta)\rangle$ using the three and four population model. Figure 5c shows that the signal expected from the species with $N \geq 3$ has excellent agreement with the onset and the overall trend of the hysteresis opening. Exclusion of the trimers shows a hysteresis onset at significantly higher coverage than the one observed. This implies that all cluster bigger than dimers contribute to the observed magnetic hysteresis, the trimers ($N = 3$) being the smallest of all. We further verified whether the MAE/atom for the $N \geq 3$ species is consistent with the observed magnetic hysteresis by extracting $K_{\geq 3}$ from the experimentally observed switching fields,[31] assuming ferromagnetic exchange coupling within a cluster (see Methods). This yields $K_{\geq 3} = 2.4 \pm 0.1$ meV/atom. Such an estimation is independent of the growth model and yet is in good agreement with the value obtained from the fits to the full magnetization curves, thus confirming the consistency of our analysis. Altogether, this demonstrates that an out-of-plane magnetization with an MAE barrier of at least 7.5 meV triggers magnetic hysteresis in Er trimers at 2.5 K. However, they also exhibit quantum tunneling of the magnetization (QTM),[32,33] as becomes evident from the butterfly shapes and the absence of remanence in the hysteresis at low coverages. Only upon reaching a significant fraction of larger sizes, at $\Theta > 0.06$ ML, the feature disappears and remanence is observed.

The ferromagnetic exchange within an Er cluster creates macrospins with large total spin and MAE. This large total spin is intrinsically less sensitive to quantum fluctuations, e.g., QTM[34,35] and scattering from the conduction electrons,[4] leading to magnetic stability in the Er clusters directly adsorbed on a metal substrate at 2.5 K. This is an alternative approach to the use of symmetry-protected ground states combined with ultrathin insulating layers for stabilizing the spin of a quantum magnet, as recently demonstrated for individual Ho atoms on MgO.[36]

In conclusion, we have demonstrated that the easy magnetization axis of Er on Cu(111) changes from in-plane for the single atoms and dimers to out-of-plane for trimers and bigger clusters. The observed change in the easy axis occurs due to the modified ligand field environment induced by the increased atomic coordination.[18] The out-of-plane magnetization, in combination with an MAE barrier of 2.5 meV/atom allows a trimers' magnetic relaxation time of 2 min at 2.5 K and 0.1 T. Together with Fe trimers on Pt(111),[6] the Er trimers on Cu(111) reported here constitute the smallest surface-adsorbed clusters exhibiting magnetic bistability.

Methods. *Sample Preparation.* The Cu(111) single crystal was cleaned in situ by several Ar^+ sputtering (4 μA/cm^2, 300 K, 1.2 keV, 30 min) and annealing cycles (up to 800 K for 20 min). Clean substrates were transferred into the cryostat (for XMCD measurements) or into the STM chamber (for low-temperature STM measurements) without breaking the vacuum. For the XMCD measurements, we evaporated Er from an e-beam evaporator with a high purity Er rod (99.99%) onto the substrate held at about 4 K inside the cryostat in a background pressure of $\lesssim 3 \times 10^{-11}$ mbar. For the low temperature STM measurements, the deposition was done from a similar Er rod after the sample was transferred into the STM chamber and was kept at either $T_d = 4 \pm 1$ K or 10 ± 1 K at a background pressure of 1.5×10^{-10} mbar. The Er rods were degassed for at least 100 h prior to the deposition, and no change in the base pressure was observed by switching on or off the evaporator. The Er flux and deposition times were carefully controlled to obtain different coverages on the surface.

XAS and XMCD Measurements. All XAS and XMCD spectra were recorded with circularly polarized light in total electron yield (TEY) mode, in an external magnetic field of 6.8 T, at 2.5 K, and in ultra high vacuum ($P_{cryo} \leq 3\times 10^{-11}$ mbar) at the EPFL/PSI X-Treme beamline at the Swiss Light Source.[10] The spectra were normalized with respect to the total intensity of the incident X-rays measured using a metal grid. Further normalization with respect to the absorption pre-edge at 1385 eV was done in order to account for the different TEY at different angles of incidence. The total XAS was calculated from the sum of the two circular polarizations and the XMCD from their difference (Figure S10b). To isolate the contribution of Er from the background of Cu(111), XAS of the clean surface within the Er $M_{4,5}$ edges were subtracted from the XAS of Er (Figure S10a). The X-Treme end station is equipped with a variable temperature STM with which we mapped the area of the substrate covered by Er for a high coverage sample. From this we derived the coverage calibration in physical monolayer (Er atoms/substrate atom) taking the different covalent radius of Er and Cu into account. This established a link between total Er XAS and coverage Θ.

Magnetization curves were recorded measuring the maximum XMCD of the M_5 edge at 1392.7 eV, normalized by the corresponding values of the XAS pre-edge. The XMCD maxima are proportional to the total magnetic moment/atom. However, this measurement does not account for the total contribution from the entire $M_{4,5}$ edge. Therefore, we normalized the magnetization curves from both incidences separately such that their ratio at 6.8 T equals to the corresponding ratio of $\langle M_{tot}\rangle$ which were obtained from the sum rules.

Semiclassical Magnetic Moment and Anisotropy of Different Er Species. The description of magnetic moment and effective anisotropy barrier for quantum systems such as single atoms and small clusters is conventionally done using an effective-spin Hamiltonian formalism.[4,5] However, the presence of differently sized clusters at each coverage would require a separate set of exchange and crystal field parameters for each size group. Therefore, the fitting of the magnetization curves using an effective-spin Hamiltonian approach would be largely overparametrized. As a convenient alternative, we adopt a semiclassical approach (see eq 2) where we assume ferromagnetic exchange coupling among the atoms within a

DOI: 10.1021/acs.nanolett.5b05214
Nano Lett. 2016, 16, 3475−3481

cluster, and we replace the whole set of crystal field parameters with an average value of the magnetic anisotropy/atom.[7] Er single crystals are ferromagnetically ordered[16] below 19 K. Also note that, all magnetic clusters are considered as isolated and noninteracting objects since substrate mediated RKKY interactions among them are expected to be at least 10 times lower[6] than what is known for transition metals.[37] Therefore, they can be safely neglected for the temperature and magnetic fields used in this work. Within these assumptions, the magnetization curve of an ensemble of Er atoms and cluster reads:

$$M(B, \theta_0) = \sum_{N=1,2,\geq 3} Q_N(\Theta)\tilde{M} \times \frac{\int_0^{2\pi} d\phi \int_0^{\pi} \sin\theta \cos\theta \exp(E(B, \theta_0, \theta, \phi)/k_B T) d\theta}{\int_0^{2\pi} d\phi \int_0^{\pi} \sin\theta \exp(E(B, \theta_0, \theta, \phi)/k_B T) d\theta} \quad (2)$$

where

$$E(B, \theta_0, \theta, \phi) = \bar{N}_N(\Theta)\tilde{M}B \cos\theta + \bar{N}_N(\Theta)K_N (\sin\theta_0 \sin\theta \cos\phi + \cos\theta_0 \cos\theta)^2 \quad (3)$$

Here, $Q_N(\Theta)$ were obtained from the growth model. The azimuthal and polar coordinates, respectively ϕ and θ, define the orientation of the semiclassical total magnetic moment/atom $\tilde{M}$, which can be interpreted as the equivalent of $g\sqrt{J(J+1)}$, and θ_0 defines the orientation of the B field with respect to the surface normal.

The total energy of a species is the sum of the Zeeman and uniaxial anisotropy terms (see eq 3). The classical MAE/atom for a species of average size $\bar{N}_N(\Theta)$ is given by K_N. The average cluster size is 1 for the monomers and 2 for the dimers, while $\bar{N}_{\geq 3}$ was quantified in a coverage-dependent manner from our STM images, i.e., $\bar{N}_{\geq 3} = 3.1 \pm 0.1, 3.5 \pm 0.1, 3.7 \pm 0.1$, and 4.1 ± 0.3 atoms, respectively for $\Theta = 0.02$, 0.032, 0.047, and 0.06 ML. Here a positive (negative) K_N indicates an out-of-plane (in-plane) anisotropy.

According to the growth model, 99.6% of the Er is in the form of monomers at 0.006 ML. Therefore, to quantify the semiclassical magnetic moment and anisotropy of the monomers, we performed a simultaneous fit to the full magnetization curves acquired at 0.006 ML using eq 2. We obtain $\tilde{M} = 9.5 \pm 0.2\ \mu_B$ and an in-plane magnetic anisotropy $K_1 = -9.9 \pm 0.9$ meV. This $\tilde{M}$ is in perfect agreement with the theoretical value of $g\sqrt{J(J+1)} = 9.6\ \mu_B$ with $J = \frac{15}{2}$ and $g = 1.2$. Since J remains constant irrespective of the cluster size, and so does the semiclassical magnetic moment/atom $\tilde{M}$, we fix $\tilde{M} = 9.5\ \mu_B$ for all size groups as the one found for the monomers. With this, we extracted the MAE/atom of the dimers (K_2) and bigger clusters ($K_{\geq 3}$) from a simultaneous fit of the magnetization curves for $\Theta = 0.015$, 0.035, and 0.045 ML for the two angles of incidence.

Magnetic Anisotropy of the Clusters Estimated from the Switching Fields. An estimation of $K_{\geq 3}$ was made independent of the growth model and by using only the experimentally observed switching fields,[31] defined as

$$H_{switch} = \frac{2K_{\geq 3}}{\tilde{M}}\left(1 - \sqrt{\frac{k_B T}{\bar{N}_{\geq 3}(\Theta)K_{\geq 3}} \log\frac{t}{\tau_0}}\right) \quad (4)$$

Here, H_{switch} is the field at which the hysteresis closes, and t defines the time required for the acquisition of a magnetization curve between 0 T and H_{switch} which is 2.7 min in our case. Knowing $\tilde{M}$ and $\bar{N}_{\geq 3}(\Theta)$ and assuming the prefactor[38] $\tau_0 = 10^{-10}$ s, we obtain $K_{\geq 3} = 2.4 \pm 0.1$ meV/atom.

■ ASSOCIATED CONTENT

Supporting Information

The Supporting Information is available free of charge on the ACS Publications website at DOI: 10.1021/acs.nanolett.5b05214.

Schematic of the data analysis, details of the low-temperature STM measurements, and growth models; a description of XAS and XMCD data analysis, additional XAS and XMCD spectra, magnetization curves, and a table containing $\langle L \rangle$, $\langle 2S \rangle + \langle 6T \rangle$ for different coverages, and multiplet calculations (PDF)

■ AUTHOR INFORMATION

Corresponding Author

*E-mail: harald.brune@epfl.ch.

Author Contributions

A.S. and F.D. contributed equally to this work.

Notes

The authors declare no competing financial interest.

■ ACKNOWLEDGMENTS

We acknowledge funding from the Swiss National Science Foundation (SNSF): No. 200020_157081/1, and 200021_146715/1. J.D. and C.W. gratefully acknowledge funding by an SNSF Ambizione Grant (No. PZ00P2 142474). We would like to acknowledge A. Uldry and B. Delley for providing us with the updated version of the multiX software.

■ REFERENCES

(1) Brune, H.; Gambardella, P. Atomic and Molecular Magnets on Surfaces. In *Fundamentals of Picoscience*; Sattler, K. D., Ed.; CRC Press Taylor & Francis Group: London, 2013; pp 447−470.

(2) Gambardella, P.; Dallmeyer, A.; Maiti, K.; Malagoli, M. C.; Eberhardt, W.; Kern, K.; Carbone, C. *Nature* **2002**, *416*, 301−304.

(3) Loth, S.; Baumann, S.; Lutz, C. P.; Eigler, D. M.; Heinrich, A. J. *Science* **2012**, *335*, 196−199.

(4) Khajetoorians, A. A.; Baxevanis, B.; Hübner, C.; Schlenk, T.; Krause, S.; Wehling, T. O.; Lounis, S.; Lichtenstein, A.; Pfannkuche, D.; Wiebe, J.; Wiesendanger, R. *Science* **2013**, *339*, 55−59.

(5) Spinelli, A.; Bryant, B.; Delgado, F.; Fernández-Rossier, J.; Otte, A. F. *Nat. Mater.* **2014**, *13*, 782−785.

(6) Steinbrecher, M.; Sonntag, A.; dos Santos Dias, M.; Bouhassoune, M.; Lounis, S.; Wiebe, J.; Wiesendanger, R.; Khajetoorians, A. A. *Nat. Commun.* **2016**, *7*, 10454.

(7) Gambardella, P.; Rusponi, S.; Veronese, M.; Dhesi, S. S.; Grazioli, C.; Dallmeyer, A.; Cabria, I.; Zeller, R.; Dederichs, P. H.; Kern, K.; Carbone, C.; Brune, H. *Science* **2003**, *300*, 1130−1133.

(8) Skomski, R.; Sellmyer, D. J. *J. Rare Earths* **2009**, *27*, 675−679.

(9) Donati, F.; Singha, A.; Stepanow, S.; Wäckerlin, C.; Dreiser, J.; Gambardella, P.; Rusponi, S.; Brune, H. *Phys. Rev. Lett.* **2014**, *113*, 237201.

(10) Piamonteze, C.; Flechsig, U.; Rusponi, S.; Dreiser, J.; Heidler, J.; Schmidt, M.; Wetter, R.; Calvi, M.; Schmidt, T.; Pruchova, H.;

DOI: 10.1021/acs.nanolett.5b05214
Nano Lett. 2016, 16, 3475−3481

Krempasky, J.; Quitmann, C.; Brune, H.; Nolting, F. J. *J. Synchrotron Radiat.* **2012**, *19*, 661−674.
(11) Thole, B. T.; van der Laan, G.; Fuggle, J. C.; Sawatzky, G. A.; Karnatak, R. C.; Esteva, J.-M. *Phys. Rev. B: Condens. Matter Mater. Phys.* **1985**, *32*, 5107−5118.
(12) Kaindl, G.; Kalkowski, G.; Brewer, W. D.; Perscheid, B.; Holtzberg, F. *J. Appl. Phys.* **1984**, *55*, 1910.
(13) Thole, B. T.; van der Laan, G.; Sawatzky, G. A. *Phys. Rev. Lett.* **1985**, *55*, 2086−2088.
(14) Thole, B. T.; Carra, P.; Sette, F.; van der Laan, G. *Phys. Rev. Lett.* **1992**, *68*, 1943−1946.
(15) Carra, P.; Konig, H.; Thole, B. T.; Altarelli, M. *Phys. B* **1993**, *192*, 182−190.
(16) Green, R. W.; Legvold, S.; Spedding, F. H. *Phys. Rev.* **1961**, *122*, 827−830.
(17) Pacchioni, G. E.; Gragnaniello, L.; Donati, F.; Pivetta, M.; Autès, G.; Yazyev, O. V.; Rusponi, S.; Brune, H. *Phys. Rev. B: Condens. Matter Mater. Phys.* **2015**, *91*, 235426.
(18) Rinehart, J. D.; Long, J. R. *Chem. Sci.* **2011**, *2*, 2078−2085.
(19) Uldry, A.; Vernay, F.; Delley, B. *Phys. Rev. B: Condens. Matter Mater. Phys.* **2012**, *85*, 125133.
(20) Dreiser, J.; Westerström, R.; Piamonteze, C.; Nolting, F.; Rusponi, S.; Brune, H.; Yang, S.; Popov, A.; Dunsch, L.; Greber, T. *Appl. Phys. Lett.* **2014**, *105*, 032411.
(21) Knorr, N.; Brune, H.; Epple, M.; Hirstein, A.; Schneider, M.; Kern, K. *Phys. Rev. B: Condens. Matter Mater. Phys.* **2002**, *65*, 115420.
(22) Zhang, X. P.; Miao, B. F.; Sun, L.; Gao, C. L.; Hu, A.; Ding, H. F.; Kirschner, J. *Phys. Rev. B: Condens. Matter Mater. Phys.* **2010**, *81*, 125438.
(23) Negulyaev, N. N.; Stepanyuk, V. S.; Niebergall, L.; Bruno, P.; Pivetta, M.; Ternes, M.; Patthey, F.; Schneider, W.-D. *Phys. Rev. Lett.* **2009**, *102*, 246102.
(24) Silly, F.; Pivetta, M.; Ternes, M.; Patthey, F.; Pelz, J. P.; Schneider, W.-D. *Phys. Rev. Lett.* **2004**, *92*, 016101.
(25) Cao, R.; Zhang, X.; Miao, B.; Zhong, Z.; Sun, L.; You, B.; Hu, A.; Ding, H. *Surf. Sci.* **2013**, *610*, 65−69.
(26) Schuh, T.; Miyamachi, T.; Gerstl, S.; Geilhufe, M.; Hoffmann, M.; Ostanin, S.; Hergert, W.; Ernst, A.; Wulfhekel, W. *Nano Lett.* **2012**, *12*, 4805−4809.
(27) Pivetta, M.; Pacchioni, G. E.; Schlickum, U.; Barth, J. V.; Brune, H. *Phys. Rev. Lett.* **2013**, *110*, 086102.
(28) Sperl, A.; Kröger, J.; Néel, N.; Jensen, H.; Berndt, R.; Franke, A.; Pehlke, E. *Phys. Rev. B: Condens. Matter Mater. Phys.* **2008**, *77*, 085422.
(29) Brune, H. *Surf. Sci. Rep.* **1998**, *31*, 125−229.
(30) Venables, J. A.; Spiller, G. D. T.; Hanbücken, M. *Rep. Prog. Phys.* **1984**, *47*, 399−459.
(31) Ouazi, S.; Wedekind, S.; Rodary, G.; Oka, H.; Sander, D.; Kirschner, J. *Phys. Rev. Lett.* **2012**, *108*, 107206.
(32) Mannini, M.; Pineider, F.; Sainctavit, P.; Danieli, C.; Otero, E.; Sciancalepore, C.; Talarico, A. M.; Arrio, M.-A.; Cornia, A.; Gatteschi, D.; Sessoli, R. *Nat. Mater.* **2009**, *8*, 194−197.
(33) Mannini, M.; Bertani, F.; Tudisco, C.; Malavolti, L.; Poggini, L.; Misztal, K.; Menozzi, D.; Motta, A.; Otero, E.; Ohresser, P.; Sainctavit, P.; Condorelli, G. G.; Dalcanale, E.; Sessoli, R. *Nat. Commun.* **2014**, *5*, 4582.
(34) Garanin, D. A.; Chudnovsky, E. M. *Phys. Rev. B: Condens. Matter Mater. Phys.* **1997**, *56*, 11102−11118.
(35) Gatteschi, D.; Sessoli, R. *Angew. Chem., Int. Ed.* **2003**, *42*, 268−297.
(36) Donati, F.; et al. *Science* **2016**, *352*, 318−321.
(37) Khajetoorians, A. A.; Wiebe, J.; Chilian, B.; Lounis, S.; Blügel, S.; Wiesendanger, R. *Nat. Phys.* **2012**, *8*, 497−503.
(38) Wernsdorfer, W.; Orozco, E. B.; Hasselbach, K.; Benoit, A.; Barbara, B.; Demoncy, N.; Loiseau, A.; Pascard, H.; Mailly, D. *Phys. Rev. Lett.* **1997**, *78*, 1791−1794.

DOI: 10.1021/acs.nanolett.5b05214
Nano Lett. 2016, 16, 3475−3481

Supporting Information:

Magnetic Hysteresis in Er trimers on Cu(111)

Aparajita Singha,[†,¶] Fabio Donati,[†,¶] Christian Wäckerlin,[†] Romana Baltic,[†] Jan Dreiser,[†,‡] Marina Pivetta,[†] Stefano Rusponi,[†] and Harald Brune[*,†]

Institute of Physics, École Polytechnique Fédérale de Lausanne, Station 3, CH-1015 Lausanne, Switzerland, and Swiss Light Source, Paul Scherrer Institute, CH-5232 Villigen PSI, Switzerland

E-mail: harald.brune@epfl.ch

Flowchart of our data analysis

Figure S1 summarizes the work flow for the data analysis. By applying the sum rules to the XMCD spectra, we obtain the total magnetization of the Er cluster ensemble as a function of coverage Θ and angle with respect to the surface normal θ. From STM measurements, we get the abundance of the three cluster-size classes: monomers ($N = 1$), dimers ($N = 2$), and larger clusters ($N \geq 3$). Since the coverages investigated with the STM do not coincide with, and are not as numerous as the ones investigated by XMCD, we apply mean-field nucleation theory to get continuous functions to describe the amounts of Er present in the form of monomers (Q_1), dimers (Q_2), and larger clusters ($Q_{\geq 3}$). Using these functions, we subsequently fit the coverage-dependent total magnetic moments $\langle M_{tot}(\Theta)\rangle$ with the expectation value of the moment/atom for each cluster-size class ($\langle M_N\rangle$, $N \in 1, 2, \geq 3$) as free parameters. In addition, from the fits of the magnetization curves at

[*]To whom correspondence should be addressed
[†]Institute of Physics, École Polytechnique Fédérale de Lausanne, Station 3, CH-1015 Lausanne, Switzerland
[‡]Swiss Light Source, Paul Scherrer Institute, CH-5232 Villigen PSI, Switzerland
[¶]Contributed equally to this work

both incident angles and various coverages, we get the magnetic anisotropy energy/atom for each size class $(K_N, N \in 1, 2, \geq 3)$. Details of the nucleation and growth model, as well as additional XMCD data, are presented in the following sections of this supporting information.

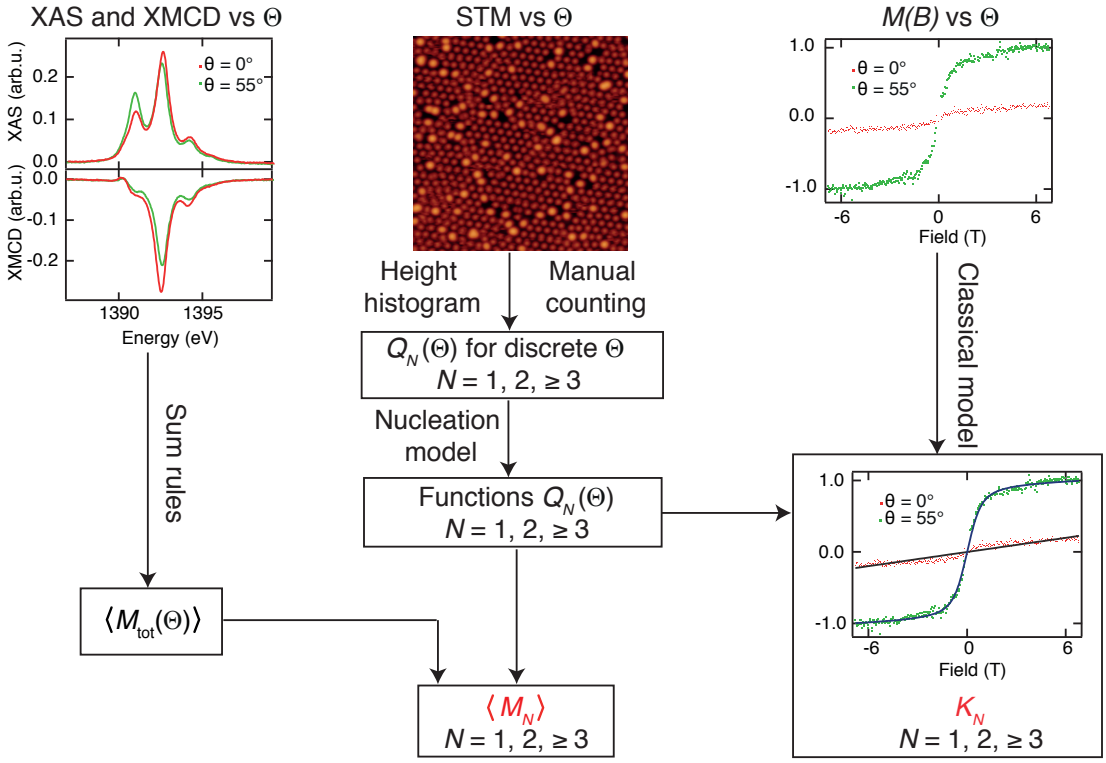

Figure S1: A sketch showing the different steps involved in the data analysis. Θ stands for the coverage in ML, $Q_N(\Theta)$ denotes the relative amount of Er present in clusters containing N number of atoms, $\langle M_{\rm tot}(\Theta)\rangle$ is the expectation value of the total magnetic moment for discrete coverages Θ obtained from the sum rule analysis. $\langle M_N\rangle$ and K_N are the expectation value of the magnetic moment and anisotropy per atom for clusters of size N.

Low temperature STM measurements

Relative abundance of different Er species

Figure S2a shows an example of an apparent height histogram extracted from an STM image using our home-made image analysis software that identifies the protrusions and evaluates their apparent height with respect to the surrounding terrace. One clearly discerns three apparent height classes corresponding to monomers ($N = 1$), dimers ($N = 2$), and clusters larger than dimers ($N \geq 3$).

Moreover, the shape analysis (Figure 4a) allows us to distinguish and therefore to quantify the densities of differently sized clusters corresponding to the $N \geq 3$ peak. With this, we estimated the Er coverage (defined as Er atoms/substrate atom) for all samples within 0.02 ML$\leq \Theta \leq$ 0.06 ML. From the linear dependence between Θ and deposition time, we deduce the deposition flux F (Figure S2b) which allows us to extrapolate the coverage for samples with $\Theta < 0.02$ ML, where imaging of the monomers is very challenging due to their high mobility on the surface. The same was applied for $\Theta > 0.06$ ML, where the presence of larger clusters prevents a direct coverage determination.

Finally, to obtain $Q_N(\Theta)$ for $N \in 1,2$, we calculate the relative amount of Er in units of atoms for a given coverage Θ. To obtain $Q_{\geq 3}$ we calculated $(1 - Q_1(\Theta) - Q_2(\Theta))$. For applying the four population nucleation and growth model, we calculate $Q_3(\Theta)$ separately for the trimers and $Q_{\geq 4}(\Theta)$ is obtained as $(1 - Q_1(\Theta) - Q_2(\Theta) - Q_3(\Theta))$.

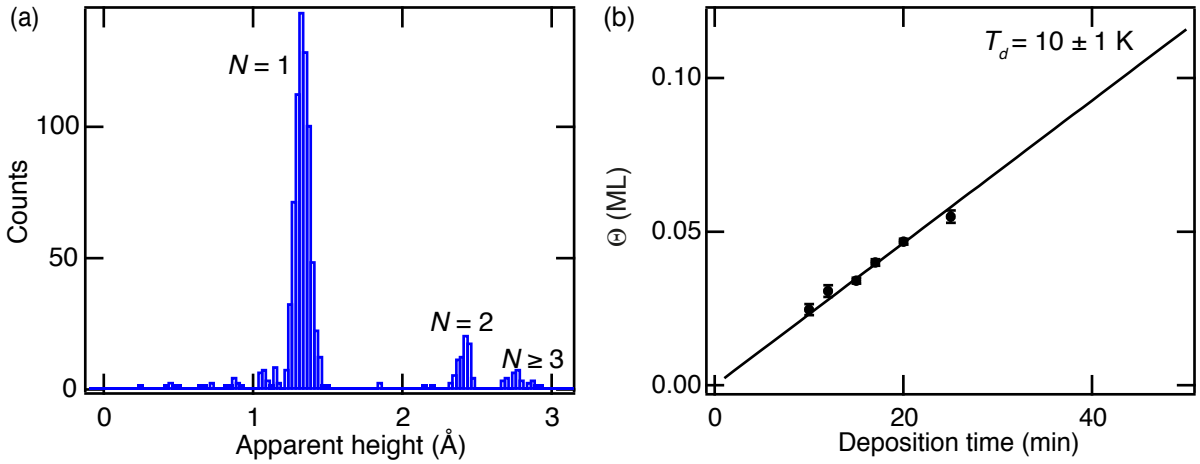

Figure S2: (a) Apparent height histogram of the Er related protrusions obtained from a 0.032 ML sample. (b) Coverage as a function of deposition time. Dots: measurements, solid line: linear fit providing $F = (2.30 \pm 0.03) \times 10^{-3}$ ML/min and allowing extrapolation of the coverage for $\Theta < 0.02$ ML and $\Theta > 0.06$ ML.

Three population nucleation and growth model

The three population nucleation and growth model relies on the following three rate equations from mean-field nucleation theory:

$$\frac{dn_1}{d\Theta} = 1 - 2\kappa_1 n_1 - \kappa_2 n_2 - \kappa_{\geq 3} n_{\geq 3} - \frac{\sigma \nu_0}{F} \exp\left(\frac{-E}{k_B T_d}\right) n_1 (n_2 + n_{\geq 3}) \tag{S1}$$

$$\frac{dn_2}{d\Theta} = \kappa_1 n_1 - \kappa_2 n_2 - \frac{\sigma \nu_0}{F} \exp\left(\frac{-E}{k_B T_d}\right) n_1 n_2 \tag{S2}$$

$$\frac{dn_{\geq 3}}{d\Theta} = \kappa_2 n_2 - 2n_{\geq 3}\left(1 - \frac{dn_1}{d\Theta} - \frac{dn_2}{d\Theta}\right) + \frac{\sigma \nu_0}{F} \exp\left(\frac{-E}{k_B T_d}\right) n_1 n_2 \tag{S3}$$

These equations express the growth rates of the species containing $1, 2$ and ≥ 3 atoms as a function of coverage Θ. Conventionally these rates are expressed with respect to time. Here we divide them by the deposition flux F. This is allowed if most of the nucleation and growth takes place during deposition, *i.e.*, post deposition processes are negligible. This is a legitimate approximation for our case since we cool down the samples immediately after deposition of Er and this cooling takes much shorter time (≈ 2 min) than the typical time for the deposition (> 5 min). Also note that it is sufficient to cool down by a few kelvin in order to suppress the post deposition processes since the respective rates depend exponentially on temperature.

The densities of the different species are expressed as n_1, n_2 and $n_{\geq 3}$. The cluster formation due to direct impingements onto adatoms or stable clusters is described through the $\kappa_N n_N$ terms. Here κ_N is the impingement cross-section of an island of size N that captures deposited adatoms by direct impingement.[1] The thermally induced growth of clusters by the lateral attachment of monomers during deposition is described through $\frac{\sigma \nu_0}{F} \exp\left(\frac{-E}{k_B T_d}\right)$, where σ defines the capture rates, ν_0 the attempt frequency, and E the effective attachment barrier.[1] To account for the experimentally observed decrease in $n_{\geq 3}$ beyond 0.10 ML, we have included a coalescence term[1,2] $\left(-2n_{\geq 3}\left(1 - \frac{dn_1}{d\Theta} - \frac{dn_2}{d\Theta}\right)\right)$.

We have neglected lateral attachment of monomers to each other by thermal diffusion due to the observed strong repulsion amongst them. This assumption is further justified because: (i) we

did not observe any dimer formation during the acquisition of STM images even though the single atoms are quite mobile under the STM tip and are only stabilized by the superlattice, (ii) at the lowest coverages, the density of dimers is not affected by the deposition temperature up to 10 K, indicating a large effective monomer-to-monomer attachment barrier. However, dimer formation through direct impingement onto monomers has to be included in order to model the observed dimer abundance. In the following, we show that this mechanism is central for proper modeling of the nucleation and growth of Er clusters.

The impingement cross-sections are defined by the number of sites around a given species where the impinging atoms directly lead to cluster formation or growth. We obtained $\kappa_1 = 7, 19, 37$ and $\kappa_2 = 12, 28, 50$ by counting for the 1^{st}, 2^{nd} and 3^{rd} nearest neighbor (NN) sites respectively. For $N \geq 3$, we computed $\kappa_{\geq 3}$ by considering a geometric approach.[1,3] The average cluster size of $N \geq 3$ clusters is given by $\langle S_{\geq 3} \rangle = \frac{\Theta - n_1 - 2n_2}{n_{\geq 3}}$. The corresponding radius of the direct impingement zone $r = \sqrt{\frac{2\langle S_{\geq 3} \rangle}{\pi}} + \frac{\alpha\sqrt{3}}{2}$. The factor of 2 in the first term accounts for the ratio of the atomic volumes of Er to Cu while $\frac{\alpha\sqrt{3}}{2}$ accounts for the distance up to the α^{th} NN sites. Finally the impingement cross-section of a cluster of average size $\langle S_{\geq 3} \rangle$ is computed as $\kappa_{\geq 3} = \pi r^2$ (Figure S3).

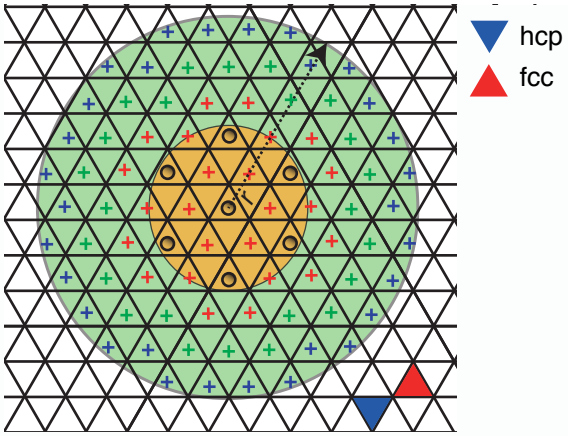

Figure S3: Schematic showing the effective impingement cross-section (in green) of a heptameter considering up to the 3rd nearest neighbor sites. The substrate is shown as a black grid. We have considered only the fcc adsorption sites (triangles pointing up). Red, green and blue crosses define respectively the 1^{st}, 2^{nd}, and 3^{rd} nearest neighbor sites. The small circles indicate the positions of the Er atoms forming the heptamer.

As can be seen from Figures S4 (a-c), none of the direct impingement models, irrespective of

the NN distances considered, can reproduce the experimentally observed trends. This deviation is due to the formation of the Er superlattice which is stabilized by the repulsive interactions between the adatoms. This lattice markedly changes the nucleation behavior. The very low dimer density

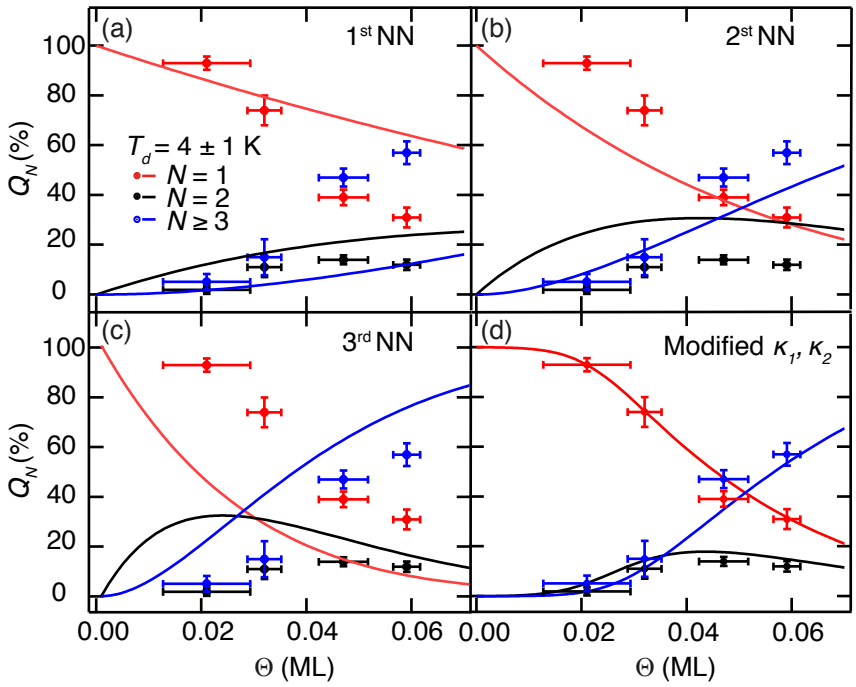

Figure S4: Relative amount of Er present in the respective cluster sizes obtained from STM (dots) in comparison with simulations considering respectively 1st, 2nd and 3rd nearest neighbor (NN) attachment areas for $N \leq 2$ (a-c) and with their attachment areas modified using Eq. S4 (d) ($T_d = 4 \pm 1$ K).

for $\Theta \leq 0.025$ ML indicates that direct attachment to monomers is ineffective in this coverage regime and that until the completion of the superlattice, the monomers can rearrange themselves in order to accommodate new atoms on the surface. The monomers which are pushed away in this process may either find empty sites or nearby dimers, which, differently from the monomers, are immobile (Figure S5). Once the complete superlattice is formed, the monomers are locked in their positions and, thus are forced to form dimers if impinged directly. This implies: (i) a coverage-dependent impingement coefficient for monomers that is reduced at low Θ and increases up to a maximum value when the superlattice is formed, (ii) monomers and dimers have a shared impingement coefficient to account for the probability of a monomer to be repelled by another monomer and to be eventually captured by a dimer. We rescaled the value of κ_1 using $G(\Theta) =$

$\frac{1-\exp(-m\Theta)}{1+\exp(-m(\Theta-\frac{\Theta_0}{2}))}$, with Θ_0 being the ideal superlattice coverage, and introduced $\kappa_S \times G(\Theta)$ as the shared attachment area:

$$\begin{cases} \widetilde{\kappa_1} = (\kappa_1 - \kappa_S) \times G(\Theta) \\ \widetilde{\kappa_2} = \kappa_2 + \kappa_S \times G(\Theta) \end{cases} \tag{S4}$$

These altogether render the coverage-dependent variation in the modified attachment areas $\widetilde{\kappa_1}$ and $\widetilde{\kappa_2}$ respectively within $(0,\ \kappa_1 - \kappa_S)$ and $(\kappa_2,\ \kappa_2 + \kappa_S)$. We obtain best agreement with experiment assuming $\kappa_1 = 37$, $\kappa_2 = 50$, which define attachment zones up to the third nearest neighbor sites.

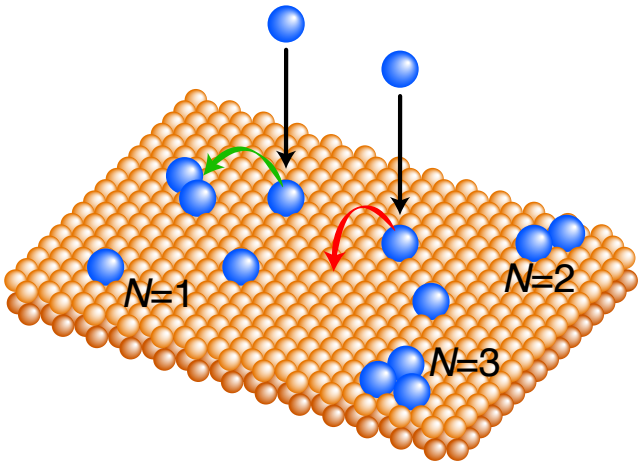

Figure S5: Schematic illustrating that, due to the inherent dipolar repulsion among monomers, atoms are pushed away on direct impingements either to an empty site (red arrow) or towards a nearby dimer (green arrow).

Using $\nu_0 = 10^{12}$ s^{-1} and assuming $\sigma = 7$ for all sizes ≥ 2 atoms,[1] we solved Eq. S1-S3 for $n_1(\Theta)$, $n_2(\Theta)$, and $n_{\geq 3}(\Theta)$. From them we determine the relative amount of Er present in clusters of size 1, 2, and ≥ 3 as: $Q_1(\Theta) = \frac{n_1(\Theta)}{\Theta}$, $Q_2(\Theta) = \frac{2n_2(\Theta)}{\Theta}$ and $Q_{\mathrm{N}\geq 3}(\Theta) = 1 - (Q_1(\Theta) + Q_2(\Theta))$. A simultaneous fit of the $Q_N(\Theta)$ derived from the STM apparent height histograms at $T_d = 4 \pm 1$ K provide the fitting parameters $m = 200$ ML^{-1}, $\Theta_0 = 0.044$ ML and $\kappa_S = 21$. $\widetilde{\kappa_1}$ approaches its maximum at the onset of superlattice formation Θ_0 (Figure S6a). The coverage Θ_0 is also in fair agreement with our STM measurements and with the ideal coverage of the superlattice (0.035 ML) that can be estimated from the NN Er distance of 1.38 ± 0.05 nm. The effective monomer-to-cluster attachment barrier E becomes important only for 10 ± 1 K deposition where the available

thermal energy helps to exceed adatom-cluster repulsion leading to an enhancement of the cluster growth by lateral attachment. We determined $E = 27 \pm 4$ meV, through the simultaneous fitting of the $Q_N(\Theta)$ obtained from the 10 ± 1 K dataset, keeping the values of m, Θ_0 and κ_S the same as determined before. On the contrary, dimer formation is not affected by increasing the deposition temperature up to 10 K, therefore the adatom-adatom attachment barrier needs to be higher than E. Finally we counterchecked the validity of this nucleation and growth model by reproducing the experimentally observed trend of the cluster density for $N \geq 3$ (Figure S6b). The model correctly follows the experimental measurements and deviates only beyond ≈ 0.10 ML, possibly due to the inherent limitations of mean-field nucleation theory in describing coalescence.[4]

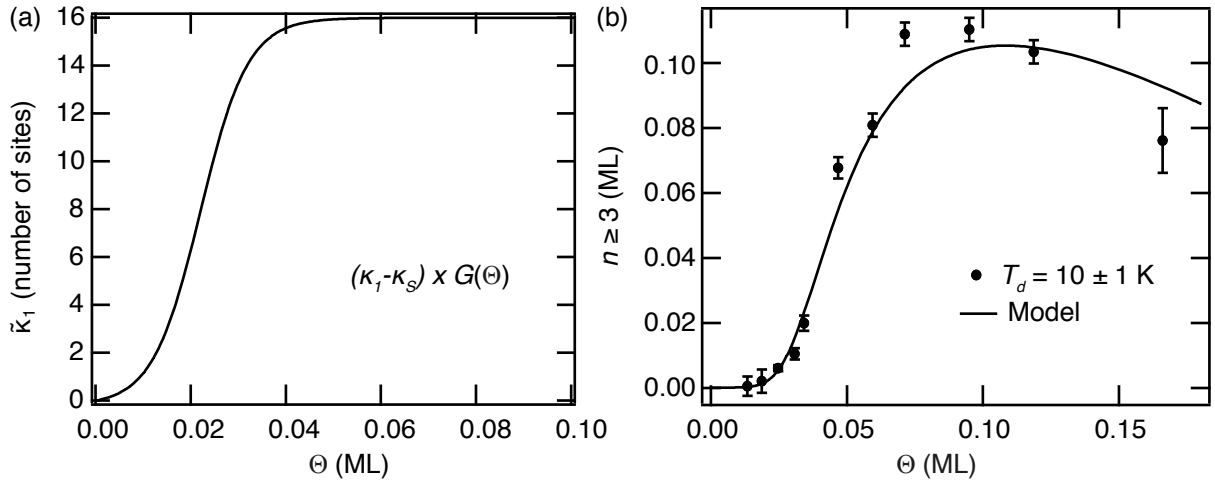

Figure S6: (a) Coverage dependence of $\widetilde{\kappa}_1$. (b) Density of the trimers and bigger clusters ($n_{\geq 3}$) as a function of coverage.

Four population nucleation and growth model

The underlying principle behind the four population model relies on the distinction between trimer and bigger clusters. The rate equations used for this model are:

$$\frac{dn_1}{d\Theta} = 1 - 2\widetilde{\kappa}_1 n_1 - \widetilde{\kappa}_2 n_2 - \kappa_3 n_{\geq 3} - \kappa_{\geq 4} n_{\geq 4} - \frac{\sigma \nu_0}{F} \exp\left(\frac{-E}{k_B T_d}\right) n_1 (n_2 + n_3 + n_{\geq 4}) \tag{S5}$$

$$\frac{dn_2}{d\Theta} = \widetilde{\kappa}_1 n_1 - \widetilde{\kappa}_2 n_2 - \frac{\sigma \nu_0}{F} \exp\left(\frac{-E}{k_B T_d}\right) n_1 n_2 \tag{S6}$$

$$\frac{dn_3}{d\Theta} = \widetilde{\kappa_2} n_2 - \kappa_3 n_3 - \frac{\sigma \nu_0}{F} \exp\left(\frac{-E}{k_B T_d}\right) n_1 (n_3 - n_2) \tag{S7}$$

$$\frac{dn_{\geq 4}}{d\Theta} = \kappa_3 n_3 - 2n_{\geq 4}\left(1 - \frac{dn_1}{d\Theta} - \frac{dn_2}{d\Theta} - \frac{dn_3}{d\Theta}\right) + \frac{\sigma \nu_0}{F} \exp\left(\frac{-E}{k_B T_d}\right) n_1 n_3 \tag{S8}$$

The attachment areas $\widetilde{\kappa_1}$ and $\widetilde{\kappa_2}$ were calculated using Eq. S4 and $\kappa_3 = 58$, obtained by counting up to the third nearest neighbor sites. For computing $\kappa_{\geq 4}$, we applied the generic approach based on effective radii calculation as described in the previous section. We used the previously found values of the relevant parameters κ_S, m, Θ_0 and E to reproduce the trends of $Q_N(\Theta)$ as described before (Figure S7). To further verify the consistency of this model, we counterchecked the out-of-plane orientation of the trimer magnetization by fitting $\langle M_{tot}(\Theta)\rangle$ using $\langle M_3\rangle$ and $\langle M_{\geq 4}\rangle$ as the fit parameters (Figure S8). To avoid overparametrization, we used fixed values of $\langle M_1\rangle$ and $\langle M_2\rangle$, extracted from the three population model. We obtain $\langle M_3\rangle = 7.2 \pm 0.2$ μ_B/atom, and $\langle M_{\geq 4}\rangle = 7.1 \pm 0.2$ μ_B/atom for $\theta = 0^\circ$ and $\langle M_3\rangle = 5.8 \pm 0.2$ μ_B/atom, and $\langle M_{\geq 4}\rangle = 5.3 \pm 0.2$ μ_B/atom for $\theta = 55^\circ$. The larger moment of the trimers in the out-of-plane direction proves that the trimer is the threshold size where out-of-plane magnetization appears.

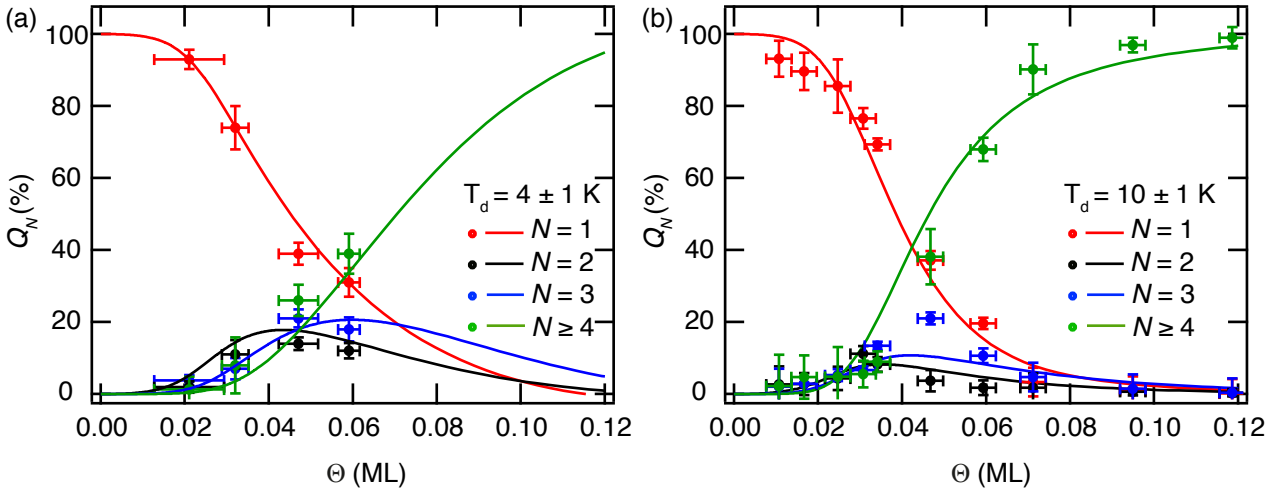

Figure S7: Coverage dependence of Q_N, the fraction of Er present in N-sized cluster for Er deposition at (a) 4 K and (b) 10 K. Dots: experiments; solid lines: fits from the four population growth model.

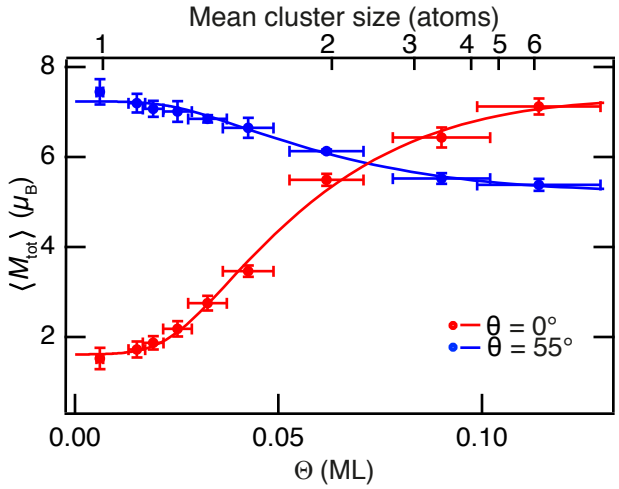

Figure S8: Coverage-dependent total out-of-plane (0°) and close to in-plane (55°) magnetic moments using four population nucleation and growth model. Dots: experiment; solid lines: fits.

Monomer magnetization curves

Figure S9 shows the magnetization curves for 0.006 ML for the two angles of incidence together with semiclassical fits. According to the growth model, at this coverage 99.6% of the Er is in the form of monomers. Therefore, these magnetization curves give exquisite access to their magnetic properties. Note that this coverage is amongst the smallest ones ever investigated with XMCD.[5,6] For the semiclassical magnetic moment ($\widetilde{M}$) and anisotropy (K_1) of the monomers we find $\widetilde{M} = 9.5 \pm 0.2\ \mu_B$ and $K_1 = -9.9 \pm 0.9$ meV.

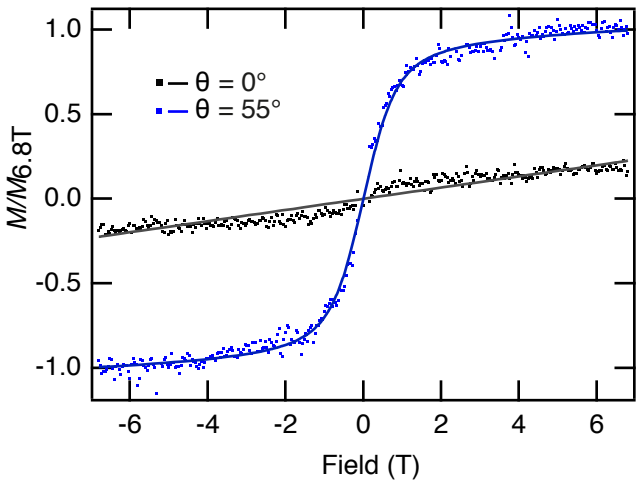

Figure S9: Magnetization curves at 0.006 ML, where the sample has predominantly monomers. Dots: measurements; solid lines: semiclassical fits ($T = 2.5$ K).

The moment $\widetilde{M}$ can be interpreted as the semiclassical equivalent of $g\sqrt{J(J+1)}$. This should not be directly compared with the $\langle M_{tot} \rangle$ obtained from the sum rules, which is instead a component of the total moment projected along the beam. Similarly, the classical anisotropy barrier K_1 should be interpreted as an estimate of the energy between the lowest and the highest state within a given multiplet for systems with purely uniaxial anisotropy. Hence this is not comparable to the zero field splitting (ZFS) which corresponds to the energy difference between ground state and first excited state.

Analysis of XAS and XMCD data

Figure S10 illustrates the steps involved in the analysis of the raw XAS and XMCD data. The x-ray absorption spectra for both circular polarizations are obtained at the Er $M_{4,5}$ edge before and after the deposition of Er. The former is used as the background (top spectra of Figure S10a) which is subtracted from the latter (middle spectra of Figure S10a) in order to obtain the signal coming from Er only. These background corrected spectra (bottom spectra of Figure S10a) are used to calculate the total absorption signal, XAS which is the sum of the absorption of the two polarizations, and the dichroism, XMCD which is the difference. Finally, sum rules are applied on such XAS and XMCD spectra (top and bottom spectra of Figure S10b respectively). To discard any spurious contribution, we have chosen the regions marked with dashed boxes centered around the $M_{4,5}$ edges for calculating the sum rules (Figure S10b).

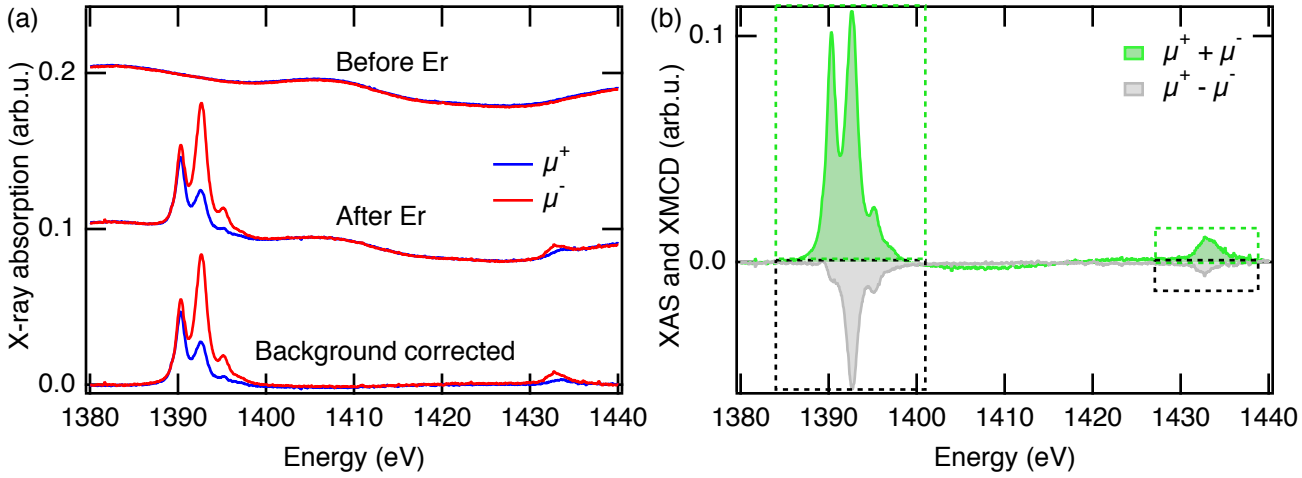

Figure S10: (a) X-ray absorption spectra for both circular polarizations at Er $M_{4,5}$ edge obtained before (top) and after (middle) the deposition of Er. Respective background corrected spectra are shown at the bottom. All spectra are offset for clarity. (b) XAS and XMCD signals obtained from the sum (green) and the difference (grey) of the absorptions of the two polarizations. Respective boxes with dotted borders indicate the regions within which the spectra were integrated in order to apply the sum rules.

Additional XAS and XMCD data

The spectra of the $M_{4,5}$ edge of Er are shown in Figure S11 for several Er coverages. Table S1 shows the values of orbital and effective spin magnetic moments obtained by applying sum rules to the corresponding XAS and XMCD spectra assuming $n_h = 3$.

Table S1: Expectation values of orbital and effective spin magnetic moments/atom in μ_B ($n_h = 3$).

Θ (ML)	$\langle L \rangle$ $\theta = 0°$	$2\langle S \rangle + 6\langle T \rangle$ $\theta = 0°$	$\langle L \rangle$ $\theta = 55°$	$2\langle S \rangle + 6\langle T \rangle$ $\theta = 55°$
0.006	0.78 ± 0.19	0.74 ± 0.14	4.09 ± 0.09	3.37 ± 0.27
0.015	0.73 ± 0.14	0.99 ± 0.11	3.97 ± 0.15	3.23 ± 0.14
0.02	0.88 ± 0.11	0.98 ± 0.12	3.89 ± 0.13	3.18 ± 0.12
0.025	1.28 ± 0.10	0.90 ± 0.14	3.83 ± 0.13	3.18 ± 0.18
0.035	1.49 ± 0.10	1.27 ± 0.13	3.89 ± 0.07	2.96 ± 0.05
0.045	1.93 ± 0.09	1.53 ± 0.09	3.75 ± 0.13	2.89 ± 0.18
0.06	3.07 ± 0.10	2.43 ± 0.09	3.42 ± 0.03	2.71 ± 0.03
0.09	3.61 ± 0.14	2.82 ± 0.16	3.11 ± 0.09	2.40 ± 0.08
0.11	3.96 ± 0.12	3.16 ± 0.14	2.94 ± 0.09	2.44 ± 0.09

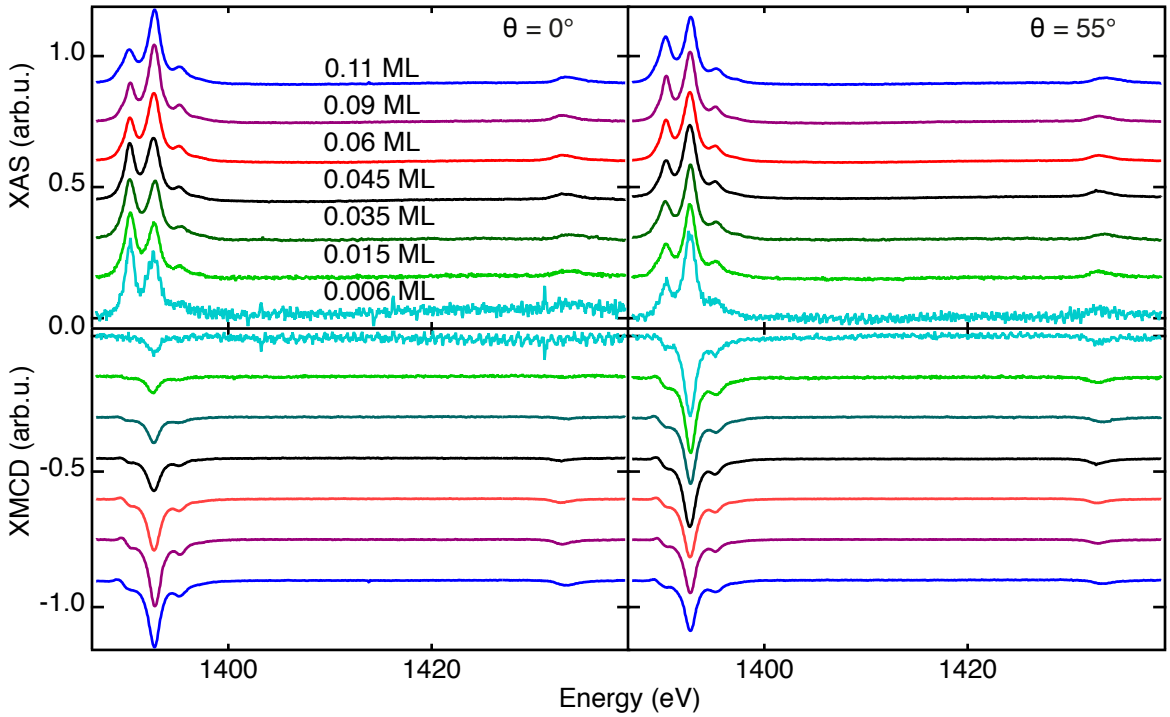

Figure S11: Coverage-dependent XAS and XMCD measurements for out-of-plane (left) and close to in-plane (right) x-ray incidence and magnetic field. The spectra are normalized to the integrated XAS and offset for clarity ($T = 2.5$ K, $B = 6.8$ T).

Multiplet calculations

The magnetic ground state of an Er cluster is determined by the interplay of two interactions, (a) the electrostatic interaction of the $4f$ shell with the surrounding ligands (Cu as well as Er) and, (b) the exchange coupling between the $4f$ electrons via the external $6s$ and $5d$ electrons of Er. Although, the latter plays an important role and is known to induce complex magnetic phases in the late lanthanide single crystals,[7] investigating this aspect is extremely demanding and far beyond the scope of this work. Therefore, we limited our analysis by involving only the interaction of an Er atom with the surrounding ligand charges. To verify the role of the ligand fields in governing the easy axis of magnetization for different clusters, we have performed atomic multiplet simulation with a point charge approach for the crystal field (CF) description using multiX software.[8] Our simulations provide a direct access to the energy levels of the ground state and first excited state multiplets. All simulations were performed for $T = 2.5$ K, with a number of holes $n_h = 3$, and

by replacing the ligands as effective point charges in the middle of the two interacting atoms. The values of the spin-orbit coupling and coulomb interactions for Er were scaled to 97% and 85% of the Hartree-Fock values, respectively. The experimental line broadening due to the finite lifetime of the core-hole state was modeled by convolution with a Gaussian of $\sigma = 0.3$ eV.

In the low coverage limit most of the population is in the form of monomers and their spectrum can be simulated by modeling a single Er atom in an effective CF given by the ligand charges of the underlying Cu(111) substrate. We compared this simulation with the spectra measured at 0.015 ML where $Q_1 \geq 97\%$. A very good agreement between the measured and calculated spectra of the single atoms (Figure S12a) is obtained by applying least-squares fits to optimize z position and the charge of the effective Cu ligands (Table S2). After applying sum rules on the simulated spectra we have obtained $\langle M_{\mathrm{tot}} \rangle = 1.6\ \mu_{\mathrm{B}}$ for $\theta = 0^\circ$ and 8.1 μ_{B} for $\theta = 55^\circ$, in good agreement with our experimental measurements (Table 1).

At the very high coverage, where cluster abundance is 100%, it is reasonable to assume that the Er atoms coordinate in a closed packed arrangement. Thus, each Er atom sees the ligands of the neighboring ones in the xy plane as equatorially placed charges around. The corresponding spectra of an ensemble of fully coordinated atoms, can therefore be simulated by placing an Er atom within the CF provided by 6 equispaced equatorial ligands. In order to investigate the effects of such equatorial ligands, we have first simulated a series of spectra by varying the Er ligand charge in between $-0.05\ e$ and $-0.15\ e$ while keeping the position and strengths of the underlying Cu ligands fixed as optimized for the single atom case (Table S3). Figure S12b shows a gradual increase (decrease) of the XMCD signal in $\theta = 0^\circ$ (55°) with increasing Er ligand charge. After applying sum rules on such spectra we obtain $\langle M_{\mathrm{tot}} \rangle$ for the two angles of incidence from which we calculate $R = \frac{\langle M_{\mathrm{tot}} \rangle @ 0^\circ}{\langle M_{\mathrm{tot}} \rangle @ 55^\circ}$. Thus $R > 1$ indicates that the easy axis is oriented out-of-plane. For the given set of CF parameters, this happens when the Er ligand charge exceeds $-0.09\ e$ (Figure S12c). The trend of R versus Er ligand charge directly proves the importance of the equatorial ligands in changing the orientation of the easy axis (Figure 1f).

Finally, to quantitatively reproduce the spectrum and the magnetic moments at the high cov-

erage limit, we optimized Cu and Er ligand charge in order to fit the measurements at 0.11 ML (Figure S13). The best agreement using least-squares fits is obtained for -0.3 e of Cu and -0.4 e of Er ligand charges. To reduce the number of free parameters, we fixed the z distance of the Cu ligand charges to the ones optimized for the monomers (-1.3 Å). Note that the need of significantly large value of the Cu charge employed here as compared to the single atom case might be a direct consequence of neglecting other interactions in this simplified model e.g., the interatomic exchange within a cluster, or a different Er-Cu distance of the monomer compared to the cluster. Nevertheless, by applying sum rules on these calculated spectra we obtain $\langle M_{\mathrm{tot}} \rangle = 7.5$ μ_{B} for $\theta = 0^{\circ}$ and 5.8 μ_{B} for $\theta = 55^{\circ}$, in very good agreement with our experimental results (Table 1). Note that all grazing spectra are obtained by averaging over all possible non equivalent orientations of the probing beam with respect to a given crystal field (shown as black arrows in the inset of Figures S12b).

Table S2: Crystal field used for the multiplet simulations of an Er monomer. The x, y coordinates were chosen following the lattice parameters of bulk Cu(111).

Cu @ z $= -1.3$ Å		
x (Å)	y (Å)	Charge e
0.72	0.00	-0.07
-0.36	0.63	-0.07
-0.36	-0.63	-0.07

Table S3: Crystal field used for the multiplet simulations of a fully coordinated Er atom at the high coverage regime. The x, y coordinates were chosen following the lattice parameters of bulk Er and Cu(111). The equatorial ligand charges were varied between -0.05 e and -0.15 e while Cu ligand charge was fixed at -0.07 e for simulations shown in Figure S12b. For the simulations shown in Figure S13b, best agreement was found with -0.4 e of Er and -0.3 e of Cu ligand charges.

Cu @ z = −1.3 Å		Er ligand charge @ z = 0 Å	
x (Å)	y (Å)	x (Å)	y (Å)
0.72	0.00	0.00	1.79
−0.36	0.63	0.00	−1.79
−0.36	−0.63	1.56	0.89
		1.56	−0.89
		−1.56	0.89
		−1.56	−0.89

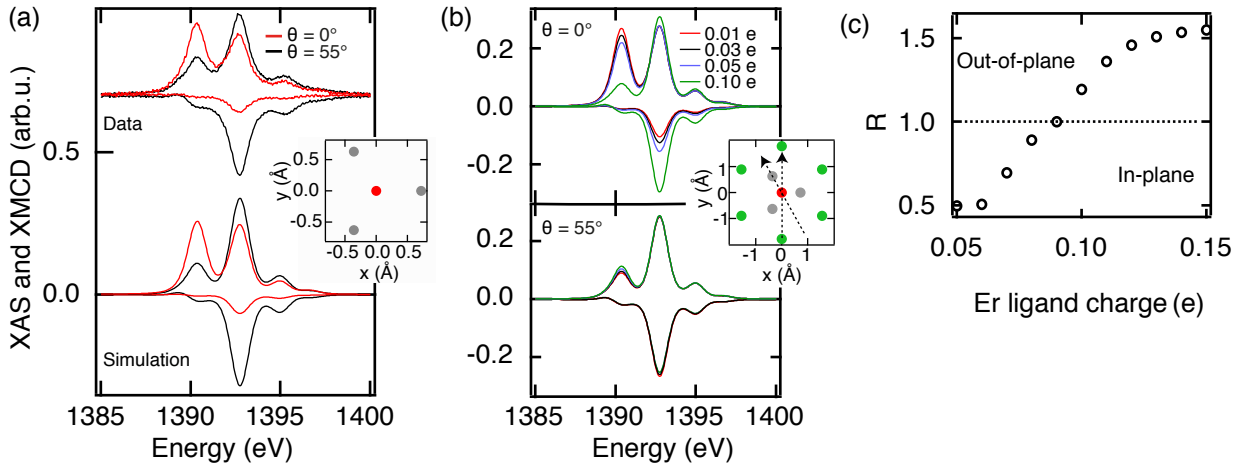

Figure S12: Multiplet calculations for an Er atom (a) in presence of only Cu ligands, and (b) with 6 additional Er ligands of varying strengths. Experimental data for 0.015 ML are also presented for comparison in (a) and are offset for clarity. In all cases the simulated spectra corresponds to the Er atom at the origin. Insets show the schematics of the crystal field; Er atoms: red, Cu ligand charge: grey, Er ligand charge: green. Arrows show the non equivalent orientations of the probing beam with respect to a given crystal field. (c) Ratio of the total moments obtained from the two angles of incident as a function of Er ligand charge.

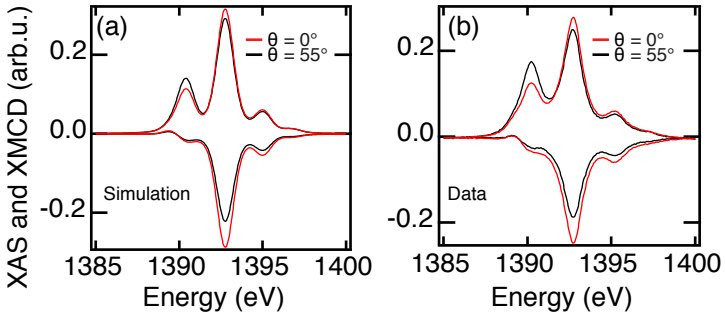

Figure S13: Multiplet calculation for an Er atom in the high coverage regime with -0.3 e of Cu and -0.4 e of Er ligand charges. The simulations are shown in (a) while the experimental data are presented for comparison in (b) with 0.11 ML.

References

(1) Brune, H. *Surf. Sci. Rep.* **1998**, *31*, 125–229.

(2) Knorr, N.; Brune, H.; Epple, M.; Hirstein, A.; Schneider, M. A.; Kern, K. *Phys. Rev. B* **2002**, *65*, 115420.

(3) Venables, J. A.; Spiller, G. D. T.; Hanbücken, M. *Rep. Prog. Phys.* **1984**, *47*, 399–459.

(4) Brune, H.; Bales, G. S.; Jacobsen, J.; Boragno, C.; Kern, K. *Phys. Rev. B* **1999**, *60*, 5991–6006.

(5) Gambardella, P.; Rusponi, S.; Veronese, M.; Dhesi, S. S.; Grazioli, C.; Dallmeyer, A.; Cabria, I.; Zeller, R.; Dederichs, P. H.; Kern, K.; Carbone, C.; Brune, H. *Science* **2003**, *300*, 1130–1133.

(6) Gambardella, P.; Dhesi, S. S.; Gardonio, S.; Grazioli, C.; Ohresser, P.; Carbone, C. *Phys. Rev. Lett.* **2002**, *88*, 047202.

(7) Hughes, I. D.; Dane, M.; Ernst, A.; Hergert, W.; Luders, M.; Poulter, J.; Staunton, J. B.; Svane, A.; Szotek, Z.; Temmerman, W. M. *Nature* **2007**, *446*, 650–653.

(8) Uldry, A.; Vernay, F.; Delley, B. *Phys. Rev. B* **2012**, *85*, 125133.